Nuclear Materials and Energy 37 (2023) 101559

Contents lists available at ScienceDirect

Nuclear Materials and Energy

journal homepage: www.elsevier.com/locate/nme

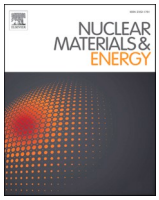

Crystal-orientation-dependent physical sputtering from four elemental metals

M. Balden [a,*], K. Schlueter [a], D. Dhard [a,b], P. Bauer [a], R. Nilsson [c], F. Granberg [c], K. Nordlund [c], G. Hobler [d]

[a] Max-Planck-Institut für Plasmaphysik, Boltzmannstraße 2, D-85748 Garching, Germany
[b] School of Engineering and Design, Technische Universität München, D-85748 Garching, Germany
[c] Department of Physics, P.O. Box 43, FIN-00014 University of Helsinki, Finland
[d] Institute of Solid-State Electronics, TU Wien, Gußhausstraße 25-25a, A-1040 Wien, Austria

ARTICLE INFO

Keywords:
Physical sputtering yield
Crystallinity
Electron backscattering diffraction (EBSD)
Focused ion beam (FIB)
Molecular dynamics (MD) simulations
Binary collision approximation (BCA) simulations

ABSTRACT

Physical sputtering and its dependence on crystal orientation is well-known, but crystallinity of the target is neither commonly considered in simulations nor when publishing experimental values for its yield. Due to the recent development of detector technology and therefore of crystal orientation mapping, a measuring technique has been established to obtain the physical sputtering yield for an extensive number of orientations of polycrystalline specimens. In this work, yields for two bcc metals (W and Mo) and two fcc metals (Cu and Pt) for impacting Ga ions with 30 keV and around 5 keV energy were determined experimentally and are compared with molecular dynamics (MD) simulations in a recently established two level approach and with binary collision approximation (BCA) simulations. The agreement between experimental yields and simulations is excellent regarding distribution in the angular space and reasonable regarding absolute values. As expected, the variation in angular space among the materials with the same crystal lattice structure is minor.

1. Introduction

Physical sputtering is one of the important erosion processes in plasma-surface interaction. It is used for many technical processes including thin film coating, precise etching, and for some analysis techniques such as depth profiling [1,2,3]. The erosion by physical sputtering of plasma-facing materials in a fusion plasma device is discussed as one of the limiting factors for the lifetime of the plasma-facing components [4,5]. For several decades, many research groups have contributed to the basic understanding of that issue [1,6,7,8], which resulted in well-established simulation techniques, e.g., the TRIM family of codes [9,10,11,12,13]. The crystallinity of the material has mostly not been considered, even though it has long been known that the physical sputtering yield can vary by more than one order of magnitude due to the crystal orientation [14]. Already in the 1960s, one of the first attempts to take crystallinity into account led to the first successful simulation code, called MARLOWE [15,16,17]. However, the vast majority of effort in code development ignored crystallinity[1]. Therefore, some aspects of the modelling still need discussion, such as: Is the assumption of an amorphous/random sample for erosion prediction by simulation programs adequate? How is the crystallinity of the material treated in the simulation programs? Are the available experimental data sufficient to validate simulations including crystallinity? In order to deliver such experimental data, we developed a measuring and evaluation strategy to obtain the physical sputtering yield for an extensive number of crystal orientations [18,19,20,21,22].

Recent developments in the detector technology for electron backscattering diffraction (EBSD), performed in a scanning electron microscope (SEM), allow the analysis of sufficiently large areas of polycrystalline samples in a reasonable time to cover huge numbers of crystal grains with different crystal orientation. Combining the EBSD data with three-dimensional profile data of the same area obtained after sputtering (e.g., by confocal laser scanning microscopy (CLSM)) resulted in sputtering yield determination for a huge number of crystal

* Corresponding author.
E-mail address: Martin.Balden@ipp.mpg.de (M. Balden).

[1] Very recently an attempt was made to implement crystallinity in the SDTrimSP [12], which will be part of the upcoming 7.0 Version, and was presented at the 19th International Conference on Plasma-Facing Material and Component, 22–25. May 2023, Bonn, Germany by U. von Toussaint and A. Mutzke, "*Simulations of sputtering, implantation and reflection properties of crystalline targets using SDTrimSP*".

https://doi.org/10.1016/j.nme.2023.101559
Received 4 August 2023; Received in revised form 17 November 2023; Accepted 18 November 2023
Available online 19 November 2023

orientations. These results can be visualized in the so-called inverse pole figure (IPF), a representation of all possible crystal orientations. For the combination of EBSD and CLSM data and their evaluation, a Python script was written [18,19,20]. In a previous study, the experimental physical sputtering yields obtained for fusion-relevant tungsten (W) bombarded by gallium (Ga) ions were compared to simulations of crystalline material with a remarkable agreement [20]. The aim of this study is to present additional experimental data for further metals with different lattice structure and to compare them with simulations.

The main focus of this study lies on the experimental method for sputtering by Ga ions with energies of 30 keV and around 5 keV for four elemental metals: two with body-centred cubic lattice structure (tungsten (W), molybdenum (Mo)) and two with face-centred cubic lattice structure (copper (Cu), platinum (Pt)). As in our previous study [20], we perform molecular dynamics (MD) and binary collision approximation (BCA) simulations of crystalline specimens in order to compare these with the experimental results. We generally find excellent qualitative and good quantitative agreement.

2. Experimental method

2.1. Experimental workflow

To obtain the physical sputtering yield for a huge number of crystal orientations, polished polycrystalline metal samples were exposed to monoenergetic ions. Ga ions of a focused ion beam (FIB) were used, i.e., a monoenergetic beam with a very small divergence. The impact angle deviation was dominated by the deflection due to scanning. The FIB and a fast EBSD detector (Oxford, Symmetry; up to 3000 pattern/s) were mounted in a SEM (FEI, Helios Nanolab 600). All materials were sputtered with 5 keV and 30 keV Ga ions at an impact angle perpendicular to the surface normal. For W, two additional energies, 2 keV and 8 keV, were used.

Before sputtering, several areas were marked by FIB and imaged with SEM to ensure the application of different microscopic techniques on the same area. The starting topography was determined by CLSM (Olympus, LEXT OSL 4000). The map of grain orientations was obtained by EBSD. The orientations are relative to the electron beam direction, as well as relative to the ion beam direction, due to the fixed angle of 52° between the electron beam and the FIB column.

Sputtering to obtain yields was then performed with a slightly defocused FIB with 18–19 nA of 30 keV Ga^+ and ~ 9nA of 5 keV Ga^+ (Table 1, column 4) for a total area in the range of 0.05 to ~ 1 mm^2 (Table 1, column 5). The area was scanned many times with the Ga beam with a pixel dwell time of 1 μs until the chosen fluence (Table 1, column 7) was reached. The required total area depends on the grain size and crystal texture of the material used, since the size of the sputtered area had to be chosen to be large enough to ensure that many crystal orientations were present in the sputtered area, while unnecessarily large experimental times were avoided. The Ga ion current used during sputtering the area varied slightly. The uncertainty of the total ion charge, which enters linearly in the yield, was assessed to be clearly below 10%. To avoid that already a second grain (with different orientation) beneath the top one was sputtered, the Ga fluence, i.e., sputtered depth must be restricted for materials with small effective grain size (see section 2.2. and Table 1, column 2). On the other hand, a high sputtered depth was desired to reduce the effect of uncertainties in sputtering yield measurement. To be able to assess that, the mean sputtered depth across the sputtered areas was obtained (Table 1., column 8). For further considerations regarding fluence, see section 2.3.1.

After sputtering, the grain orientations were mapped across the sputtered area by EBSD, which offered the ability to filter out regions with changed orientation during sputtering compared to before sputtering. Further filtering, like a noise filter and a grain boundary filter, were applied to the EBSD data. For more details on filtering, see [18,19,21]. The main information to be correlated with the grain orientation, the sputtered depth (convertible into sputtering yield), was determined by CLSM. An example of topography after sputtering is shown in Fig. 1(a). Sputtered depth could be gained already from such data by linearly interpolating the non-sputtered frame and subtracting a plane fitted to the frame. By applying difference microscopy to the topography data obtained before (with the remaining roughness after polishing) and after sputtering, the uncertainty of the sputtered depth was reduced. After applying difference microscopy, the non-sputtered part exhibited a perfect plane, except (dis-)appearance of a dust particle, and made the absolute scale for the sputtered depth accessible. By subtracting this plane, the sputtered depth map was obtained.

The filtered EBSD map and the sputtered depth map, scalable by sputtered area, FIB current, and sputtering time to physical sputtering yields, were merged via affine transformation. In addition, the Python script used for merging allowed the correction of possible misalignments of the ion beam with respect to surface normal by principal component analysis (PCA). This PCA analysis led to the best solution with an accuracy of better than 1° [19,20]. It is important to note that this accuracy enables performance of an impact angle detection [20,22]. More details to this can be found in [18,19,20,21,22]. The applied correction to the presented data was always below 5°, and in most cases only 1 to 2°. Note that the impact angle variation by the deflection of the FIB beam was for the largest areas in the same range (1-2°). An additional data treatment to take this variation into account would be possible, but

Table 1
Some experimental parameters: Parameters for obtaining the experimental data shown in Figs. 2-4 are given in columns 3–7. The total sputtering times range from 1400 to 2.2E + 5 s, i.e., these times are the proportionality factor between flux and fluence (column 6 and 7). The mean values of the sputtered depth across the area sputtered with parameters given in the same line are listed in column 8. The durations given in column 9 are the total exposure times during the complete energy sweep to obtain the secondary electron emission images. Note that the Ga ion current varied (5–19 nA) with Ga ion energy (2–30 keV). Column 10 gives the range of fluences which were used in fluence screening series normalized to the value given in column 7. Column 11 gives the factor by which the effective Ga ion flux density was increased in the flux screening test compared to the value given in column 6, i.e., the one used for obtaining the sputtering yield data shown in Figs. 2-4. The effective grain size given in column 2 was estimated from SEM images and EBSD maps taking the distortions inside the grains into account.

1	2	3	4	5	6	7	8	9	10	11
Metal	Effective grain size (μm)	Ga impact energy (keV)	Ga ion beam current (nA)	Sputtered area (μm^2)	Effective flux density (at $m^{-2}\ s^{-1}$)	Fluence (at m^{-2})	Observed mean depth (μm)	Duration SE series (s)	Screening test: relative fluence variation	Screening test: factor of flux increase
W	30	30	18.6	860 × 690	2.E + 17	1.E + 22	0.85	2100	1/2–4	64
		5	9.0	850 × 650	1.E + 17	2.E + 22	0.95		1/2–2	64
Mo	~1	30	18.5	270 × 220	2.E + 18	3.E + 21	0.2	420	1/2–1.5	64
		5	9.2	270 × 220	1.E + 18	8.E + 21	0.15		1/8–2	260
Cu	~1	30	18.6	240 × 200	2.E + 18	4.E + 21	0.35	2400	1/4–4	260
		5	9.0	240 × 200	1.E + 18	2.E + 22	0.5		1/8–2	260
Pt	>100	30	18.2	900 × 750	2.E + 17	6.E + 21	0.6	5000	1/5–2	270
		5	9.0	900 × 750	8.E + 16	1.E + 22	0.5		1/4–5	–

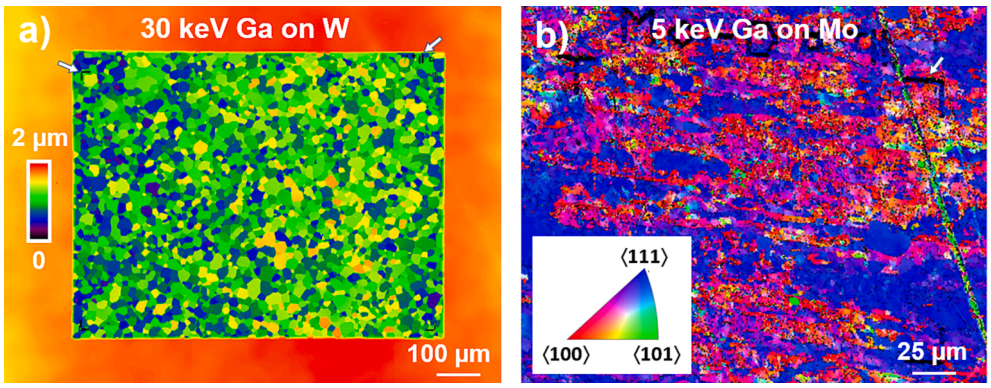

Fig. 1. a) Surface topography of W specimen after sputtering by 30 keV Ga ions obtained by CLSM. b) Orientation map of the evaluated area of the Mo specimen for obtaining the sputtering yield data shown in Fig. 3a by 5 keV Ga ions. The orientations are colour-coded in respect to the surface normal. Note that in both images the markers for area identification are visible in black, marked partially by white arrows.

is not included in the present evaluation program.

The resulting physical sputtering yields for a huge number of crystal orientations were plotted in an inverse pole figure (IPF). The IPF is a representation of the whole angular space. Its approximately triangular shape results from considering the symmetry of cubic crystal lattices. This reduces the azimuthal angle from 360° to 45° and the polar angle from 90° to 54.7°. Note that crystal directions are plotted in the IPF, but for cubic lattice structures (and only for cubic structures), the directions are perpendicular to the crystal planes with the same indices.

In a separate experiment on another marked and pre-characterised area, secondary electron images produced by the scanned Ga ion beam were recorded to correlate the intensity of the secondary electron emission induced by the impacting Ga ions with the physical sputtering yield. The area was bombarded by varying the Ga energy from 30 keV down to 2 keV and up to 30 keV again. A sequence of images was recorded. For each energy (2, 5, 8, 16, 30 keV), the area was scanned until the contrast stayed constant. The total durations of the energy sweeps are given in Table 1, column 9. The images at the same energy of the "down" and "up" sweep were undistinguishable. This indicates the reproducibility and, after reaching constant contrasts, the absence of any influence of the previous bombardment with a different Ga energy. For the low magnification used for the Pt specimen, a shading correction was applied to these images used to correlate grain orientation and sputtering yield. For details of the shading correction, see [21]. Theoretical modelling predicts, at least in the collision cascade regime [23,24], that the energy deposited in the top layer (say top 2 nm [20]) is proportional to the sputtering yield. It can be speculated and was proposed that the secondary electron emission is also proportional to this energy [24,25,26,27]. Stark et al. [26] suggested that secondary electron emission measurements can be used as a surrogate for the laborious physical sputtering yield determination. They proposed that, if the orientation dependence of the secondary electron yield is known as well as the yield for one orientation, the orientation dependence of the sputtering yield can be obtained by simple scaling. In order to check this hypothesis, first the intensity data for each Ga energy were merged with the respective orientation map in the same way as the physical sputtering yields. These merge data can be visualized also in an IPF. Second, the physical sputtering yield and the intensity for the same orientation were correlated.

2.2. Specimens

The used specimens were selected by their crystal structures, i.e., body-centred cubic (bcc) lattice structure and face-centred cubic (fcc) lattice structure, and by the availability of specimens at the start of the experimental campaign. Initially, the following elemental bcc and fcc metals were considered: i) tungsten (W), molybdenum (Mo), iron (Fe) and chromium (Cr), and ii) copper (Cu), platinum (Pt), gold (Au) and aluminium (Al), respectively. All specimens were small plates with a surface area of 12x15 mm^2 and a thickness of ~ 1 mm, except the Pt specimen which was even smaller. All specimens were polished to a mirror finish with a deviation from planarity of typically less than 100 nm. Vibro-polishing was applied for all metals except W, which was electro-polished after its recrystallisation with subsequent grinding. The polishing was intended to achieve high enough quality of the EBSD pattern for the automatic evaluation. Only for the W specimens a precise pre-characterisation existed beforehand, showing that the performed recrystallisation at 2000 K for 35 min led to nearly defect-free crystallites of about 30 µm in median size (see Fig. 1a) with a strong preferred orientation of ⟨1 0 0⟩ [19,28]. Thus, these W specimens were ideal polycrystals, i.e., a bunch of many, nearly defect-free single crystals with different orientations. In previous experiments, the suitability of the microstructure of these W specimens for determining the crystal-orientation-dependent physical sputtering yield was shown [19,20,21].

To explore which microstructure (i.e. crystal texture, grain sizes and distortions inside grains resulting in a smaller effective grain size) is still suitable for our method to determine the crystal-orientation-dependent physical sputtering yield, a variation in microstructure for the other metals than W was desired. The effective grain size ranged from a few micrometres for the distorted Cu and Mo specimens (see Fig. 1b), leading to even better orientation spread in the data than for W, to >100 µm for Pt with a quite restricted variation of crystal orientations present in the selected areas, which led to "white" areas in the IPFs. The effective grain sizes are given in Table 1, column 2.

As the grain size of the Au specimen was even larger (>200 µm), this specimen was cancelled from the measurements. The number of grains in the area scannable with the lowest possible magnification of the used SEM was too low, i.e., orientation maps obtained by EBSD must be stitched, and the time needed for sputtering with FIB to a reasonable depth would be too large.

The polishing quality of the Al and Fe specimens was, unfortunately, not sufficient to obtain reasonable crystal orientation data by EBSD at the start of the experimental campaign. Therefore, Al and Fe were not further pursued. In addition, Cr was not further explored because a strong effect was observed in the flux screening test for 30 keV (see section 2.3.2).

2.3. Further experimental considerations

2.3.1. Fluence dependence

An experimental check was made dealing with a possible fluence dependence of the sputtering yield. Such fluence dependence may be a result of changes

i) in the composition of multicomponent targets or by substantial implantation or chemical bonding of the projectiles [29],
ii) by the development of surface topography, e.g., due to the crystal structure [30], crystal defects leading to etch pits [31,32], or small fractions of impurities [33], or
iii) by accumulation of damage, i.e., destruction of the crystal lattice [34]).

Such fluence dependence was observed experimentally [29,35,36]. Because all of the possibilities given above except the first one might be valid for this study, fluence screening tests were performed. Note that the quality of the EBSD pattern after sputtering indicates that none of the four metals exhibited a strong damaging during sputtering. Furthermore, no hint of redeposition of material on the roughened surface was found [27].

To check whether the chosen fluence affects the measured yield, areas of the same size on the same specimen were bombarded for different times with otherwise the same FIB settings, i.e., the number of scans of the Ga beam across the area was varied, while all parameters for shaping and positioning of the Ga beam spot were fixed. The ranges of fluence variation normalized to the one used for determining the physical sputtering yields shown in Figs. 2-4 are given in Table 1, column 10. By simply using the mean sputtered depth across each area, no significant deviation from the proportionality between this sputtered depth and time (i.e. fluence) was observed for any of the four metals in these fluence ranges.

2.3.2. *Effective flux density*

To assess the influence of the effective flux density on the sputtering yield, a flux screening test was performed on all investigated materials. In this test, several areas on the same specimen of different sizes with otherwise the same FIB parameters were sputtered with 30 keV Ga and 5

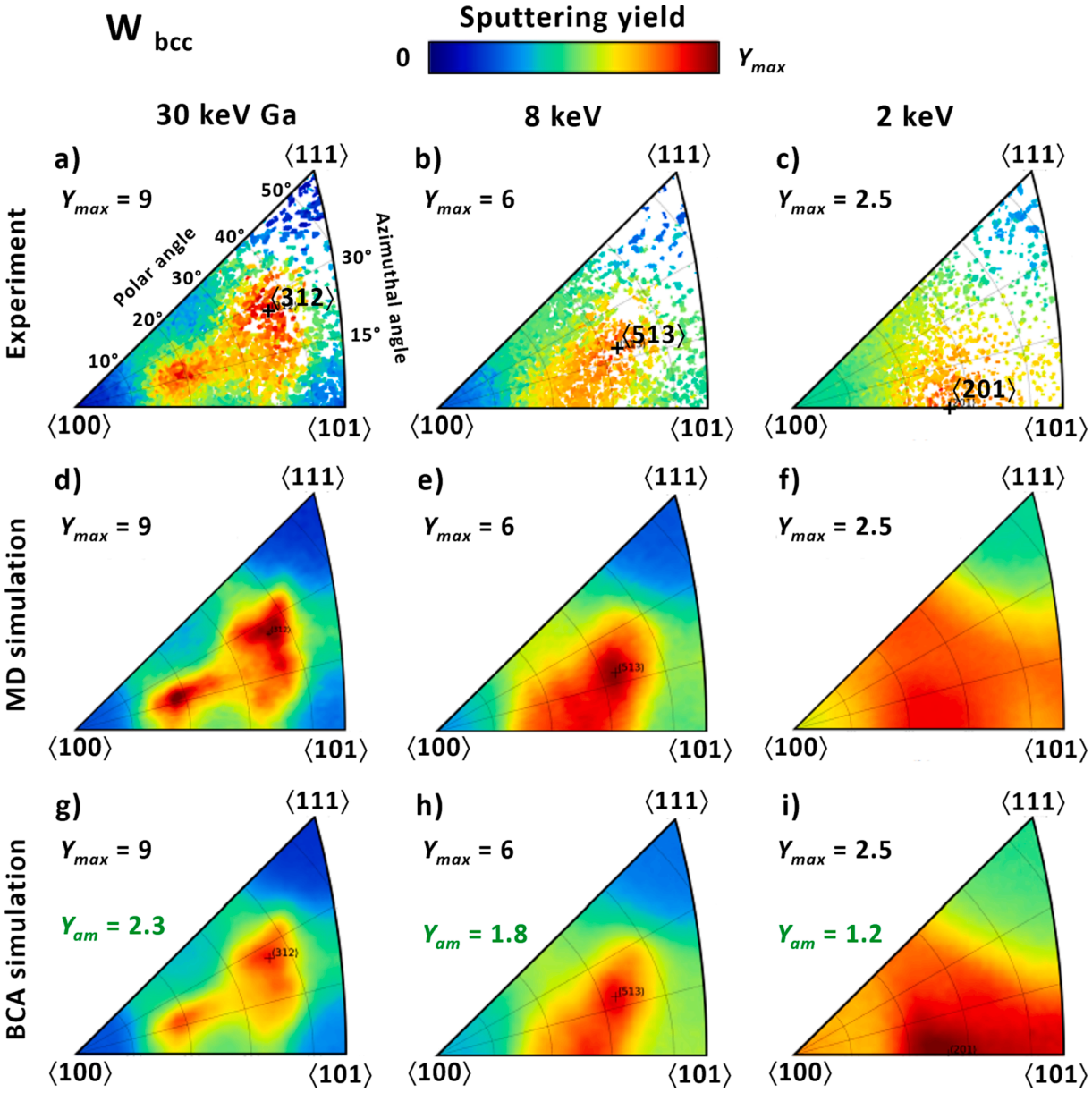

Fig. 2. IPFs of experimental (top row) and simulated physical sputtering yields using MD (middle row) and BCA (bottom row) for 30, 8, and 2 keV Ga ion bombardment (left, mid and right column, respectively) on W. The colour scaling for each energy, i.e., in each column is the same, starting from zero to the maximal sputtering yield Y_{max}, which is given in each subfigure. The Y_{am} values given in the subfigures of the last row result from BCA simulations for an amorphous (random/non-crystalline) specimen. Labelling for the polar and azimuthal angle is only given in (a).

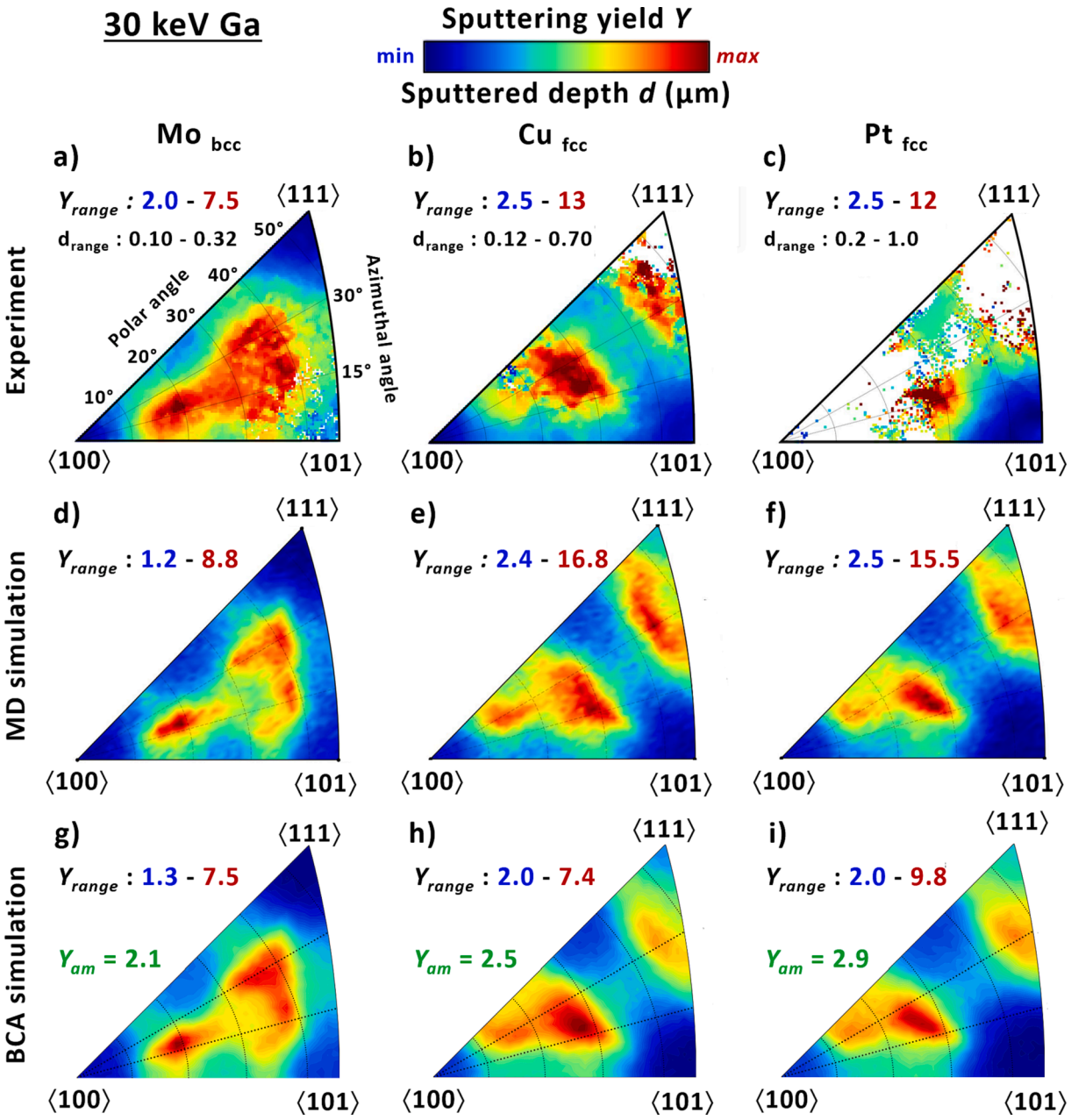

Fig. 3. IPFs of the experimental (top row) and simulated physical sputtering yields using MD (middle row) and BCA (bottom row) of Mo, Cu, and Pt (left, mid and right column, respectively) for Ga impacts with 30 keV. The range of the physical sputtering yield Y for each subfigure is different, while using the same colour coding. The individual range is given in each subfigure as Y_{range}. For experimental data, the range of the sputtered depth d_{range} are given in these subfigures, too. The Y_{am} values given in the subfigures of last row result from BCA simulations for an amorphous (random/non-crystalline) specimen. Labelling for the polar and azimuthal angle is only given in (a).

keV Ga ions up to the same fluence to verify the expected sputtered depth. Note that changing only the size of sputtered area means that the time between reaching (i.e., sputtering) again the same pixel in the area by the scanned Ga ion beam was varied, which resulted in a change of the *effective* Ga ion flux density; the flux in the beam spot stayed the same. The effective flux density should not have any effect on the sputtered depth, except for a presumable effect of oxidation by the residual gas ($<10^{-6}$ mbar). It is well known that oxides reduce the sputtering yields [37]. This effect was observed to be dramatic for Cr as the mean sputtered depth by 30 keV Ga nearly vanished (~25 nm) for the largest area of ~ 0.4 mm^2, i.e., an effective flux density of 3×10^{17} at/(m^{2}s), while it reached about the expected depth of 400 nm for ~ 0.002 mm^2, i.e., an effective flux density of 6×10^{19} at/(m^{2}s) [22]. Since the first observation of a minor influence of the effective flux density on the sputtering yield for 2 keV Ga on W [19], this screening test was performed routinely. The maximal effective flux densities used in the test normalized to the one used for the data of Figs. 2-4 are given in Table 1, column 11. If an influence of the effective flux density on the sputtering yield occurs, it can be overcome by using a higher effective flux density by composing the total area of several sequentially sputtered, sufficiently small areas, which are analysed in one CLSM and EBSD map [19,22]. This was successfully done for 2 keV Ga impacts on W shown in Fig. 2c [19], but was not needed to perform for any other data given in Figs. 2-4.

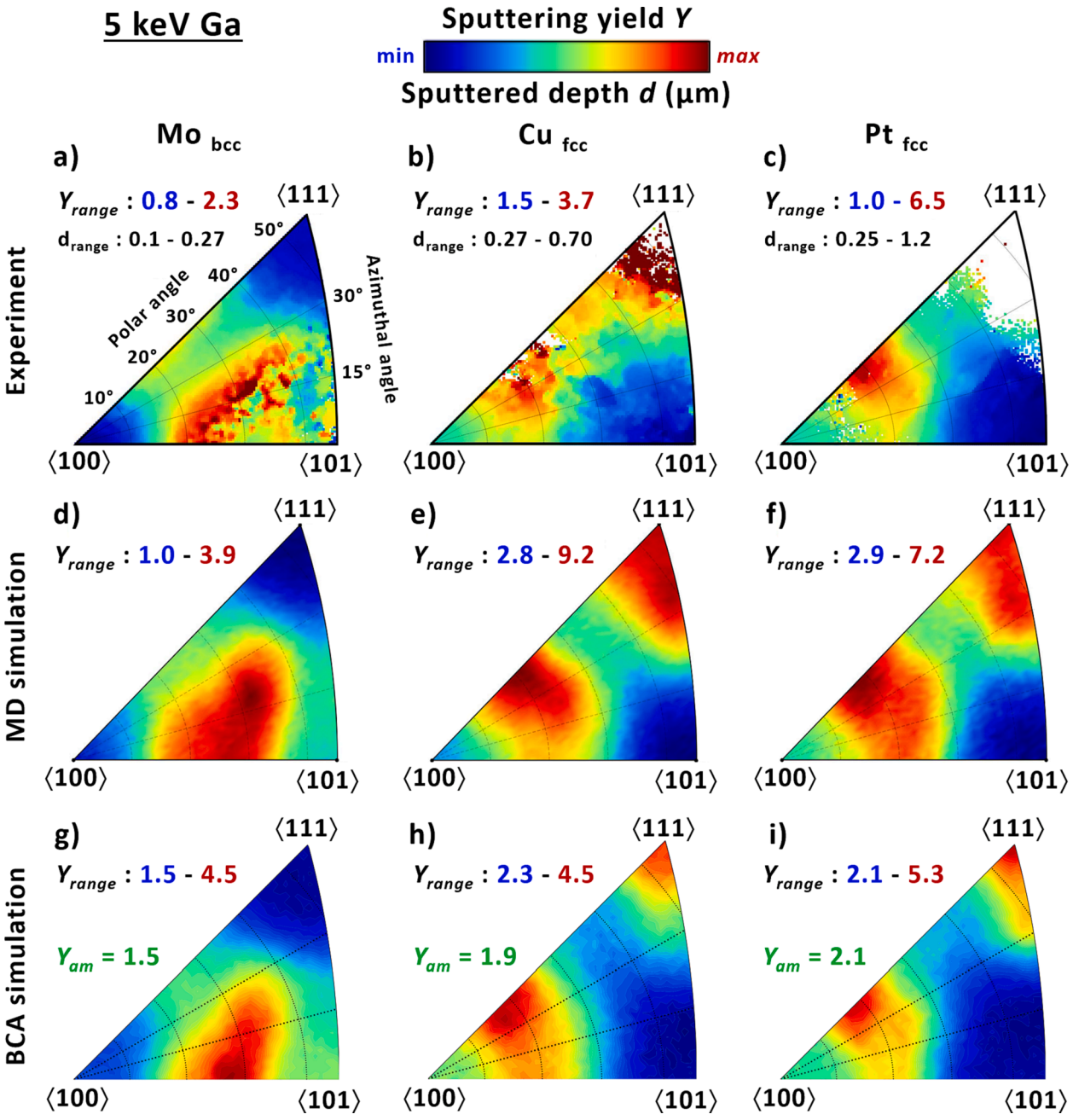

Fig. 4. IPFs as in Fig. 3, but for 5 keV Ga ion energy.

3. Simulation methods

3.1. Molecular dynamics simulations

Molecular dynamics (MD) simulations were performed in a recently established two-level approach [20]. In the first step, the full development of collision cascades for a few crystal orientations were simulated with the PARCAS code [38]. As a result, a linear dependence of sputtering yield on energy transferred to recoils was obtained. This linearity was observed for all four metals at both energies. However, simulating a sufficiently large number of orientations (>1000) representative for the whole angular space would be too time consuming. Therefore, in the second step, the recoil interaction approximation (RIA) was used to calculate the energy transferred to recoils near the surface as a function of crystal orientation with the MDRANGE code [39,40]. This energy was then converted to sputtering yield with the linear relation gained in the first step. For more details, see [20].

The dependence of the physical sputtering yields on the crystal orientation (with the surface perpendicular to it) is obtained for Ga impacts with an energy of 2, 8 and 30 keV for W (Fig. 2), and of 5 and 30 keV for Mo, Cu and Pt (Figs. 3 and 4).

3.2. Binary collision approximation

The physical sputtering yield was also obtained by applying the binary collision approximation (BCA). The BCA simulations were performed with the IMSIL code [41] for > 2000 orientations and 10,000 impacts for each orientation. The resulting IPFs of the physical sputtering yield are shown together with the results from the experiments and the MD simulations in Figs. 2-4. The yields for non-crystalline (amorphous/random) specimens were also calculated with IMSIL and are given as Y_{am} in Figs. 2-4.

The simulations were performed with the same models as in our previous work [20]. In short, the universal Ziegler-Biersack-Littmark (ZBL) potential [11] with a maximum impact parameter of 3 Å, a planar surface potential [24] with a surface binding energy equal to the heat of sublimation [12], and the electronic stopping power model of SRIM-2013 [12] were used. For local electronic stopping, the Oen-Robinson model [42] with a screening length of 5 times the ZBL screening length for the Ga ions and 4.5 times the ZBL screening length for the target atoms was employed.

4. Results and discussion

Figs. 2, 3 and 4 show the experimental IPFs together with the simulated IPFs of the physical sputtering yield of W, Mo, Cu and Pt for 5 keV and 30 keV Ga ions (2, 8, and 30 keV for W targets). The IPFs of W for 5 keV (not presented) and 8 keV are nearly identical, but with poorer statistics in the 5 keV data. In all cases, the Ga impact angle with respect to the surface normal, i.e., the crystal direction, is (about) zero. For most of the experimental data, the sputtered depth is shown, too. From the results, the following statements can be made:

i) By comparing the distributions in the angular space obtained from the experiment and the two simulations, i.e., columns in the Figs. 2-4, their agreement is striking.
ii) The distributions in the angular space for metals with the same lattice structure, bcc and fcc, under otherwise identical conditions are nearly the same. For the bcc crystals, local minima in the sputtering yield are found in ⟨1 0 0⟩ and ⟨1 1 1⟩ direction and, at 30 keV, in ⟨1 1 0⟩ direction. For the fcc crystals, the most pronounced minimum is found in ⟨1 1 0⟩ direction and a weaker minimum in ⟨1 0 0⟩ directions. In the ⟨1 1 1⟩ direction the situation is unclear in the experiment because of lacking data, while the simulations show a very weak local minimum for 30 keV, and a maximum for 5 keV.
iii) Beyond this qualitative agreement (i.e., the agreement of the pattern), the quantitative agreement of the absolute values for the bcc metals is remarkable for all energies on W (Fig. 2) and for 30 keV on Mo (Fig. 3adg). For 5 keV on Mo (Fig. 4adg), both simulations agree well and deliver a factor of about two higher yields than those measured experimentally.
iv) For the fcc metals the agreement of the absolute values is miscellaneous. While for 30 keV experiments and MD simulations agree with each other and BCA exhibits up to about a factor of 2 lower yields, experimental and BCA values for 5 keV agree but MD yields are up to a factor of two higher.
v) The distribution in the angular space becomes less structured with lower energy, e.g., see Fig. 2.

Unfortunately, at present it can only be speculated about the reasons for the deviations up to a factor of two. First, for MD simulations it is known that the used interatomic potential could have an influence on calculated physical sputtering yields [42]. Samela et al. [43] showed that the agreement depends on energy: one potential may describe experimental results better at low energies, while another one at higher energies. Therefore, other potentials for the fcc metals for the low energy case must be tried in the future.

A possible explanation for the lower sputtering yields obtained from BCA compared to MD can be given by observing that the melting point of the four elements decreases in the order W (3680 K) → Mo (2890 K) → Pt (2045 K) → Cu (1358 K), which is just the order in which the deviation between MD and BCA increases. The same applies to the heat of sublimation (often used as the surface binding energy in BCA simulations): W (8.68 eV) → Mo (6.83 eV) → Pt (5.84 eV) → Cu (3.52 eV) [11]. According to Thompson [44,45], heat spikes (which are covered by MD but not by BCA simulations) produce an additional contribution to sputtering proportional to $\exp(-E_s/kT)$, where E_s denotes the surface binding energy, T the temperature of the spike, and k Boltzmann's constant. Since Cu has by far the lowest surface binding energy, this could possibly point to heat spikes as the cause for the deviation between MD and BCA simulations.

A further possible cause for the deviations between MD and BCA simulations is the breakdown of the BCA at low energies. Note that most sputtered atoms have low energy [23], according to linear collision theory, with the maximum of the energy distribution peaking around $E_s/2$ [45]. With smaller E_s, a larger fraction of the sputtered atoms has lower energies, where the BCA tends to fail [46].

As explained end of section 2.1, it would be convenient if the physical sputtering yield is linear to the secondary emission yield by the Ga ions and if this linearity held for a significant range of sputtering conditions. The database in literature is quite small [20,25,26], but this linearity was observed for 30 keV Ga on W [20] and Fe [26]. In the study presented here, it has been found that it holds also for 30 keV Ga on Mo, but for Cu and Pt some deviations were observed for 30 keV Ga. For low energies (around 5 keV), the linearity is clearly broken. This can be seen exemplarily for 5 keV Ga on Mo in Fig. 5 showing the secondary electron emission intensity image, the respective IPF, and correlation between physical sputtering yield and emission intensity: Although in Fig. 5c some correlation of secondary electron emission by Ga impact to sputtering yield is observed, this is strongly non-linear. The orientation of each data point in Fig. 5c is colour-coded showing that only crystals with the low-index orientations, ⟨1 0 0⟩ and ⟨1 1 1⟩, exhibit a low intensity, i.e., appear dark in the secondary electron image shown in Fig. 5a. This image exhibits still a clear crystal orientation contrast. In Fig. 5b the intensity data are presented as an IPF. This IPF is completely different from the one showing the sputtering yield (Fig. 4a). Note that in case the linearity is valid, the IPFs showing sputtering yield and secondary emission intensities are undistinguishable (see [20] for W bombarded with 30 keV Ga). So, unfortunately, the range of validity of the linearity between sputtering yield and secondary electron emission by impacting Ga ions is strongly restricted.

Last but not least, it should be noted that the sputtering yield for the amorphous target Y_{am} (Figs. 2-4) does not describe a large fraction of the orientations, and Y_{am} is lower than the yield for a crystal-texture-free polycrystalline target, i.e., the mean yield value for a polycrystalline sample with random distribution of all orientations. This agrees with the findings of Ref. [20] where linear collision sequences have been identified as the most probable cause of the discrepancy.

5. Conclusion/Summary

The recently developed methodology to determine the physical sputtering yield of an extensive number of crystal orientations was applied to four elemental metals. The obtained physical sputtering yield data of W, Mo, Cu and Pt bombarded with 30 keV and around 5 keV Ga ions were compared to MD and BCA simulations. The agreement of the sputtering yield for 30 keV Ga impacts for experiment and both simulations, MD and BCA, is excellent for the distribution in the angular space as well as for the absolute experimental values. The deviation for lower energies is mainly in the absolute values, and no definitive explanation has been found yet. As expected, the distributions in angular space among the metals with the same crystal lattice structure (fcc or bcc) are very similar. As already stated in [20], the simulated physical sputtering yield for an amorphous material neither agrees with those for a large fraction of orientations nor with the value for a crystal-texture-free sample calculated from the crystal-orientation-dependent sputtering yields.

The linearity between sputtering yield and electron emission intensities only holds for 30 keV Ga bombardment on the bcc metals W and Mo. But already for 30 keV on Cu and Pt significant deviations from the linearity are observed. Furthermore, for low Ga impact energies around 5 keV, it is not valid anymore.

The excellent agreement between the physical sputtering yields of

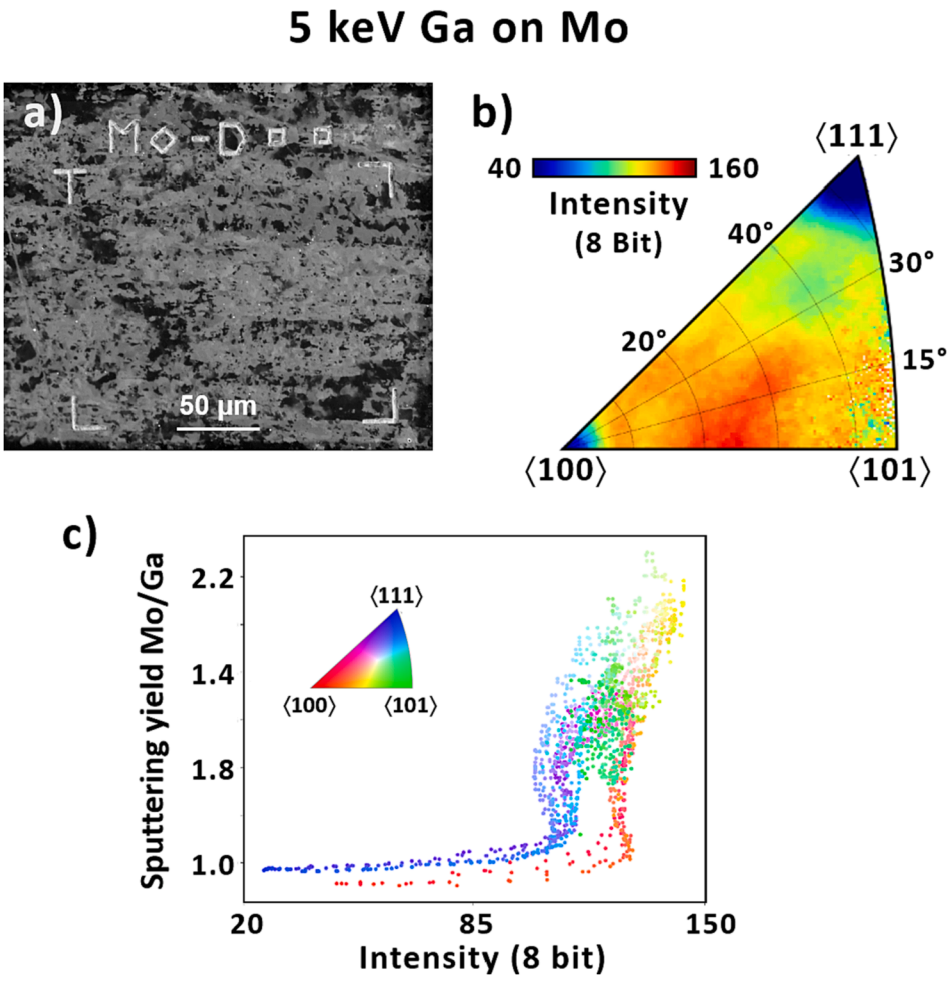

Fig. 5. a) Secondary electron image produced by 5 keV Ga ions impacting on Mo. Note that the markers for area identification are visible (white). b) IPF plot of the secondary electron emission intensity merged with the respective orientation data (not shown). This IPF deviates strongly from the one for sputtering yields shown in Fig. 4a. c) Correlation between physical sputtering yield (Fig. 4a) and secondary electron emission intensity (Fig. 5b) for the same grain orientation. The grain orientation of the correlated data points is colour-coded according to the inserted IPF. Note that the 8-bit intensity scale depends on the setting of the secondary electron detector used, i.e., represents only a relative scale.

the experiments and the two kinds of simulations confirms our confidence in the predictive power of simulations considering the crystal-orientation-dependent sputtering for other projectile-target combinations than studied here. It encourages to assess the relevance of the real crystal texture of materials in applications where sputtering is important, e.g., for plasma-facing components in fusion plasma device [4,5]).

CRediT authorship contribution statement

M. Balden: Conceptualization, Investigation, Methodology, Supervision, Visualization, Writing – original draft, Writing – review & editing. **K. Schlueter:** Conceptualization, Methodology, Investigation, Visualization. **D. Dhard:** Investigation, Visualization. **P. Bauer:** Investigation. **R. Nilsson:** Formal analysis, Visualization. **F. Granberg:** Formal analysis. **K. Nordlund:** Formal analysis, Software. **G. Hobler:** Formal analysis, Software, Visualization, Writing – review & editing.

Declaration of Competing Interest

The authors declare that they have no known competing financial interests or personal relationships that could have appeared to influence the work reported in this paper.

Data availability

Data will be made available on request.

Acknowledgments

The authors like to thank K. Hunger for preparation of the samples.

G.H. is a member of the COST Action FIT4NANO CA19140, http://www.fit4nano.eu/.

This work has partially been carried out within the framework of the EUROfusion Consortium, funded by the European Union via the Euratom Research and Training Programme (Grant Agreement No 101052200 — EUROfusion). Views and opinions expressed are however those of the author(s) only and do not necessarily reflect those of the European Union or the European Commission. Neither the European Union nor the European Commission can be held responsible for them.

References

[1] R. Behrisch, K. Wittmaack (eds.), Sputtering by Particle Bombardment III: Characteristics of Sputtered Particles, Technical Applications, Topics in Applied Physics vol. 64 (Springer, Berlin, Heidelberg, 1991).

[2] A.A. Tseng, Recent developments in micromilling using focused ion beam technology, J. Micromech. Microeng. 14 (2004) R15–R34.

[3] J.T. Gudmundsson, Physics and technology of magnetron sputtering discharges, Plasma Sources Sci. Technol. 29 (2020), 113001.

[4] C. Garcia-Rosales, Erosion processes in plasma-wall interactions, J. Nucl. Mater. 211 (1994) 202–214.
[5] G.J. van Rooij et al., Tungsten divertor erosion in all metal devices: Lessons from the ITER like wall of JET, J. Nucl. Mater. 438 (2013) S42-S47.
[6] R. Behrisch (Ed.), "Sputtering by Particle Bombardment I: Physical Sputtering of Single-Element Solids", Topics in Applied Physics, vol. 47, Springer, Berlin, Heidelberg, 1981.
[7] R. Behrisch (Ed.), "Sputtering by Particle Bombardment II: Sputtering of Alloys and Compounds, Electron and Neutron Sputtering, Surface Topography", Topics in Applied Physics, vol. 52, Springer, Berlin, Heidelberg, 1983.
[8] R. Behrisch, W. Eckstein (eds.), Sputtering by Particle Bombardment IV: Experiments and Computer Calculations from Threshold to MeV Energies, Topics in Applied Physics vol. **110** (Springer, Berlin, Heidelberg, 2007).
[9] H. Hofsäss, K. Zhang, A. Mutzke, Simulation of ion beam sputtering with SDTrimSP, TRIDYN and SRIM, Appl. Surf. Sci. 310 (2014) 134–142.
[10] J.F. Ziegler, SRIM – The Stopping and Range of Ions in Matter (Lulu Press Co., 860 Aviation Parkway; Suite 300, Morrisville, NC 27560, USA, 2015).
[11] SRIM-2013, https://www.srim.org.
[12] A. Mutzke, R. Schneider, W. Eckstein, R. Dohmen, K. Schmid, U. von Toussaint, G. Badelow, SDTrimSP version 6.00, IPP Report 2019-02, Max-Planck-Institut für Plasmaphysik (IPP) (2019).
[13] W. Möller, M. Posselt, TRIDYN-FZR User Manual, Scientific Technical Report FZR-317, Helmholtz Center Dresden Rossendorf (2002).
[14] H.E. Roosendaal in "Sputtering by Particle Bombardment I", chapter 5 "Sputtering Yields of Single Crystalline Targets", ed. R. Behrisch, Topics in Applied Physics vol. 47 (Springer, Berlin, Heidelberg, 1981).
[15] O.S. Oen, M.T. Robinson, The effect of channeling on displacement cascade theory, Appl. Phys. Lett. 2 (1963) 83–85.
[16] M.T. Robinson, I.M. Torrens, Computer simulation of atomic-displacement cascades in solids in the binary-collision approximation, Phys. Rev. **B** 9 (1974) 5008–5024.
[17] M. Hou, M.T. Robinson, Computer studies of low energy scattering in crystalline and amorphous targets, Nucl. Instr. Meth. 132 (1976) 641–645.
[18] K. Schlueter, M. Balden, T. da Silva, Dependence of oxidation on the surface orientation of tungsten grains, Int. J. Refract. Met. Hard Mater. 79 (2019) 102–107.
[19] K. Schlueter, Tungsten properties correlated with the orientation of its crystals, PhD-Thesis, IPP-Report-2021-17 (2021), https://dx.doi.org/10.17617/2.3347814.
[20] K. Schlueter, K. Nordlund, G. Hobler, M. Balden, F. Granberg, O. Flinck, T.F. da Silva, R. Neu, Absence of a crystal direction regime in which sputtering corresponds to amorphous material, Phys. Rev. Lett. 125 (2020) 225502 with Supplemental Material.
[21] D. Dhard, Grain-oriented sputtering of face centered cubic and body centered cubic metals, Bachelor Thesis, IPP-Report-2023-07 (2023), https://dx.doi.org/10.17617/2.3513468.
[22] P. Bauer, Winkeldetektion des Ionenstrahls in der SIESTA, Bachelor Thesis, IPP-Report-2023-06 (2023) (in German), https://dx.doi.org/10.17617/2.3513461.
[23] P. Sigmund in "Sputtering by Particle Bombardment I", chapter 2 Sputtering by Ion Bombardment: Theoretical Concepts, ed. R. Behrisch, Topics in Applied Physics vol. 47 (Springer, Berlin, Heidelberg, 1981).
[24] P. Sigmund, Theory of sputtering. I. Sputtering yield of amorphous and polycrystalline targets, Phys. Rev. 184 (1969) 383–416.
[25] R.E. Franklin, E.C.G. Kirk, J.R.A. Cleaver, H. Ahmed, Channelling ion image contrast and sputtering in gold specimens observed in a high-resolution scanning ion microscope, J. Mater. Sci. Lett. 7 (1988) 39–41.
[26] Y. Stark, R. Frömter, D. Stickler, H.P. Oepen, Sputter yields of single- and polycrystalline metals for application in focused ion beam technology, J. Appl. Phys. 105 (2009), 013542.
[27] B.W. Kempshall, S.M. Schwarz, B.I. Prenitzer, L.A. Giannuzzi, R.B. Irwin, F. A. Stevie, Ion channeling effects on the focused ion beam milling of Cu, J. Vac. Sci. Technol. **B** 19 (2001) 749–754.
[28] A. Manhard, M. Balden, S. Elgeti, Quantitative microstructure and defect density analysis of polycrystalline tungsten reference samples after different heat treatments, Pract. Metallogr. 52 (2015) 437–466.
[29] G. Betz, G.K. Wehner in "Sputtering by Particle Bombardment II: Sputtering of Alloys and Compounds, Electron and Neutron Sputtering, Surface Topography", chapter 2 "Sputtering of Multicomponent Materials", ed. R. Behrisch, Topics in Applied Physics vol. 52 (Springer, Berlin, Heidelberg, 1983).
[30] B.M.U. Scherzer in "Sputtering by Particle Bombardment II", chapter 7 "Development of Surface Topography Due to Gas Ion Implantation", ed. R. Behrisch, Topics in Applied Physics vol. 52 (Springer, Berlin, Heidelberg, 1983).
[31] J. Achard, F. Silva, O. Brinza, X. Bonnin, V. Mille, R. Issaoui, M. Kasu, A. Gicquel, Identification of etch-pit crystallographic faces induced on diamond surface by H_2/O_2 etching plasma treatment, Phys. Status Solidi **A** 206 (2009) 1949–1954.
[32] D. Hull, D.J. Bacon, Introduction to Dislocations, fifth ed., Elsevier, Amsterdam, Boston, 2011.
[33] G. Carter, B. Navinsek, J.L. Whitton in "Sputtering by Particle Bombardment II", chapter 6 "Heavy Ion Sputtering Induced Surface Topography Development", ed. R. Behrisch, Topics in Applied Physics vol. 52 (Springer, Berlin, Heidelberg, 1983).
[34] A. Barna, B. Pecz, M. Menyhard, Amorphisation and surface morphology development at low-energy ion milling, Ultramicrocopy 70 (1998) 161–171.
[35] M. Balden, E. de Juan Pardo, H. Maier, P. Starke, U. Fantz, Chemical erosion behaviour of doped graphites under hydrogen impact: A comparison of ion beam experiments and planar inductively coupled RF plasmas, Phys. Scripta **T** 111 (2004) 123–128.
[36] P. Blank, K.J. Wittmaack, Energy and fluence dependence of the sputtering yield of silicon bombarded with argon and xenon, J. Appl. Phys. 50 (1979) 1519–1528.
[37] W. Eckstein "Sputtering by Particle Bombardment IV", chapter 3 "Sputtering Yields", eds. R. Behrisch and W. Eckstein, Topics in Applied Physics vol. 110 (Springer, Berlin, Heidelberg, 2007).
[38] PARCAS, available open source at https://gitlab.com/acclab/parcas/.
[39] K. Nordlund, Molecular dynamics simulation of ion ranges in the l-100 keV energy range, Comput. Mater. Sci. 3 (1995) 448–456.
[40] K. Nordlund, F. Djurabekova, G. Hobler, Large fraction of crystal directions leads to ion channeling, Phys. Rev. **B** 94 (2016), 214109.
[41] G. Hobler, Monte Carlo simulation of two-dimensional implanted dopant distributions at mask edges, Nucl. Instrum. Meth. Phys. Res. **B** 96 (1995) 155–162.
[42] O.S. Oen, M.T. Robinson, Computer studies of the reflection of light ions from solids, Nucl. Instr. Meth. 132 (1976) 647–653.
[43] J. Samela, J. Kotakoski, K. Nordlund, J. Keinonen, A quantitative and comparative study of sputtering yields in Au, Nucl. Instr. Meth. **B** 239 (2005) 331–346.
[44] M.W. Thompson, R.S. Nelson, Evidence for heated spikes in bombarded gold from the energy spectrum of atoms ejected by 43 keV A+ and Xe+ ions, Phil. Mag. 7 (1962) 2015–2026.
[45] M.W. Thompson, The contribution of collision cascades to sputtering and radiation damage, Phil. Trans. Royal Soc. Lond. **A** 362 (2004) 5–28.
[46] W. Eckstein, Computer Simulation of Ion-Solid Interactions, Springer, Berlin, Heidelberg, 1991.